



Cite this: DOI: 10.1039/d2cp02690b

A global CHIPR potential energy surface of $\text{PH}_2(\text{X}^2\text{B}_1)$ via extrapolation to the complete basis set limit and the dynamics of $\text{P}(^2\text{D}) + \text{H}_2(\text{X}^1\Sigma_g^+) \rightarrow \text{PH}(\text{X}^3\Sigma^-) + \text{H}(^2\text{S})^\dagger$

Guangan Chen,^a Zhi Qin,^a Jing Li^c and Linhua Liu^{*abd}

A global potential energy surface (PES) for the electronic ground state of $\text{PH}_2(\text{X}^2\text{B}_1)$ is reported based on accurate *ab initio* energy points and analytically modeled using the combined-hyperbolic-inverse-power-representation (CHIPR) method. A total of 12 339 *ab initio* energy points are calculated by the multireference configuration interaction method with the Davidson correction and extrapolated to the complete basis set limit using the aug-cc-pV(T + d)Z and aug-cc-pV(Q + d)Z basis sets. A switching function is constructed to model the transition between $\text{P}(^2\text{D})$ and $\text{P}(^4\text{S})$ to ensure the reliable behaviors at dissociation limits. The *ab initio* potential energy curves of $\text{H}_2(\text{X}^1\Sigma_g^+)$ and $\text{PH}(\text{X}^3\Sigma^-)$ are refined by a multi-attribute fitting to previous experimental spectroscopic constants. The analytical CHIPR PES reproduces well with the *ab initio* energy points with a root mean square deviation of 41.7 cm^{-1} . The topographical features of the CHIPR PES are examined and discussed in detail, and they agree well with those of the previous work. The quasi-classical trajectory method is utilized to calculate the integral cross sections and thermal rate constants for the insertion reaction of $\text{P}(^2\text{D}) + \text{H}_2(\text{X}^1\Sigma_g^+) \rightarrow \text{PH}(\text{X}^3\Sigma^-) + \text{H}(^2\text{S})$. The results show a typical characteristic of the endothermic reaction with a barrier and this PES can be a reliable component for constructing the PESs of PH_3 or other larger molecular systems containing PH_2 .

Received 14th June 2022,
Accepted 21st July 2022

DOI: 10.1039/d2cp02690b

rsc.li/pccp

1 Introduction

The hydrides of phosphorus are of great astrophysical significance, and have been known to be present in the atmospheres of Saturn¹ and Jupiter² and also observed outside the solar system.³ The phosphino radical (PH_2) and phosphinidene (PH) are critical intermediate products in the photodissociation sequence of phosphine (PH_3),⁴ whose final product P_4 is thought to be a major cause of the Great Red Spot on Jupiter.^{5,6} Hence, the dynamic study for the PH_2 system may be helpful to investigate the chemical evolution of the P atom in interstellar space, such as the insertion reaction of $\text{P} + \text{H}_2 \rightarrow \text{PH} + \text{H}$.

The insertion reactions of H_2 with various gaseous atoms or ions have long been a focus of great interest due to their potential applications in interstellar, atmospheric and combustion chemistry. For example, the insertion mechanisms in the CH_2 ,⁷ NH_2 ,^{8,9} H_2O ,¹⁰ AlH_2 ,¹¹ and H_2S^{+12} systems had been investigated. The results show that the insertion reaction of a molecular system has a unique characteristic due to the inherent topographical feature of its potential energy surface (PES). The dynamics of the insertion reaction generally depends on the depth of the potential well and the small or null barrier on the insertion entrance.¹³ For instance, the rate constant of a barrierless insertion reaction usually exhibits a weak temperature dependence. From a theoretical point of view, a state-resolved reaction often corresponds to several PESs of different electronic states, but the main contribution generally comes from the ground-state PES.¹⁴ For the PH_2 system, the $\text{P}(^2\text{D}) + \text{H}_2(\text{X}^1\Sigma_g^+) \rightarrow \text{PH}(\text{X}^3\Sigma^-) + \text{H}(^2\text{S})$ reaction of its ground state X^2B_1 should be the main concern, although the $\text{P}(^2\text{D}) + \text{H}_2(\text{X}^1\Sigma_g^+)$ asymptote correlates with five doublet PESs of PH_2 . Note that the ground state $\text{P}(^4\text{S})$ can also react with $\text{H}_2(\text{X}^1\Sigma_g^+)$, which correlates with a PES of the excited quartet state for PH_2 .

Spectroscopic experiments of $\text{PH}_2(\text{X}^2\text{B}_1)$ can provide useful validations for the theoretical studies. On one hand,

^a School of Energy and Power Engineering, Shandong University, 250061, Jinan, China. E-mail: z.qin@sdu.edu.cn, liulinhua@sdu.edu.cn

^b Optics and Thermal Radiation Research Center, Institute of Frontier and Interdisciplinary Science, Shandong University, 266237, Qingdao, China

^c School of Physics and Physical Engineering, Qufu Normal University, 273165, Qufu, China

^d School of Energy Science and Engineering, Harbin Institute of Technology, 150001, Harbin, China

[†] Electronic supplementary information (ESI) available: The Fortran code for CHIPR PES. See DOI: <https://doi.org/10.1039/d2cp02690b>

experiments presented the spectroscopic constants of $\text{PH}_2(\text{X}^2\text{B}_1)$, such as the bending vibration frequency ω_2 and symmetrical stretching vibration frequency ω_1 , which were obtained by analyzing the absorption spectra of the bending vibration^{15–17} and symmetrical stretching vibration.^{17–19} The latest experimental vibration frequencies of $\text{PH}_2(\text{X}^2\text{B}_1)$ were measured by Jakubek *et al.*¹⁷ with the values of $\omega_1 = 2298 \text{ cm}^{-1}$ and $\omega_2 = 1102 \text{ cm}^{-1}$. On the other hand, experiments obtained the equilibrium geometries of the electronic state $\text{PH}_2(\text{X}^2\text{B}_1)$,^{20–23} which were deduced from the observed vibronic bands of the $\text{A}^2\text{A}_1\text{--X}^2\text{B}_1$ transition. The recent results were $R_{\text{PH}} = 1.4178 \text{ \AA}$ and $\theta_{\text{HPH}} = 91.69^\circ$ for the X^2B_1 state and $R_{\text{PH}} = 1.4059 \text{ \AA}$ and $\theta_{\text{HPH}} = 120.99^\circ$ for the A^2A_1 state,²² respectively. In addition, experiments also produced the dissociation energy D_0 . For HP–H, it was estimated to be $74.2 \pm 2 \text{ kcal mol}^{-1}$.²⁴

For theoretical studies, several attempts were made to calculate the equilibrium geometry of PH_2 .^{25–29} In particular, Woodcock *et al.*²⁸ calculated the equilibrium geometry for the three lowest-lying electronic states of PH_2 at 44 different levels of theory and presented accurate geometries of the X^2B_1 and A^2A_1 states. The $D_0(\text{HP–H})$ of $\text{PH}_2(\text{X}^2\text{B}_1) \rightarrow \text{PH}(\text{X}^3\Sigma^-) + \text{H}(^2\text{S})$ was calculated to be $72.2 \text{ kcal mol}^{-1}$,³⁰ which agrees well with the measured value.²⁴ Meanwhile, Kayi *et al.*²⁹ obtained the geometry and bending vibrational frequency of the linear ground state of $\text{PH}_2(^2\Pi_u)$, which was found to be a transition state in our work. However, the analytical PESs for the electronic states of PH_2 had not been investigated in the above-mentioned studies.

The first analytical PESs of the X^2B_1 and A^2A_1 states of PH_2 were constructed by Jakubek *et al.*¹⁷ and the two PESs showed a reasonable Renner–Teller degeneracy at the HPH collinear configuration. Subsequently, Yurchenko *et al.*³¹ utilized these PESs to compute the rotation–vibration structure of PH_2 . These PESs were constructed using 210 energy points in the vicinity of the equilibrium geometry of PH_2 . Zhang *et al.*³² presented an analytical PES of $\text{PH}_2(\text{X}^2\text{B}_1)$ without consideration of the conical intersection in the $\text{P}(^2\text{D}) + \text{H}_2(\text{X}^1\Sigma_g^+)$ channel. For accurate studies of the reaction dynamics, an analytically modeled global PES is required, so as to describe the relevant topological features, such as dissociation limits, barriers on the entrance channel, *etc.* Also, there has not been a dynamic study of $\text{P}(^2\text{D}) + \text{H}_2(\text{X}^1\Sigma_g^+) \rightarrow \text{PH}(\text{X}^3\Sigma^-) + \text{H}(^2\text{S})$ reported.

In this work, the main purpose is to construct a global PES for the ground state $\text{PH}_2(\text{X}^2\text{B}_1)$, so as to carry out a tentative study of $\text{P}(^2\text{D}) + \text{H}_2(\text{X}^1\Sigma_g^+) \rightarrow \text{PH}(\text{X}^3\Sigma^-) + \text{H}(^2\text{S})$. The energy points of $\text{PH}_2(\text{X}^2\text{B}_1)$ were calculated by the state-of-the-art *ab initio* methods, along with the basis set extrapolation to the complete basis set (CBS) limit. The CBS energies were then used to fit the analytical functional form of combined-hyperbolic-inverse-power-representation (CHIPR)³³ based on the many-body expansion (MBE)^{34,35} theory. The CHIPR method was proposed by Varandas³³ and recently developed by Rocha *et al.*^{36–38} and Xavier *et al.*^{39–41} The CHIPR two-body fragments of $\text{H}_2(\text{X}^1\Sigma_g^+)$ and $\text{PH}(\text{X}^3\Sigma^-)$ were refined by previous experimental spectroscopic constants. The obtained CHIPR PES was introduced to the quasi-classical trajectory (QCT)

method^{42,43} to compute the integral cross section and thermal rate constants of $\text{P}(^2\text{D}) + \text{H}_2(\text{X}^1\Sigma_g^+) \rightarrow \text{PH}(\text{X}^3\Sigma^-) + \text{H}(^2\text{S})$. It is worth mentioning that there exists a small barrier in the entrance of the PES for the ground state $\text{NH}_2(\text{X}^2\text{B}_1)$ and the electronic structure of $\text{PH}_2(\text{X}^2\text{B}_1)$ resembles that of $\text{NH}_2(\text{X}^2\text{B}_1)$. Therefore, the PES of the ground state $\text{PH}_2(\text{X}^2\text{B}_1)$ may have similar topographical features to $\text{NH}_2(\text{X}^2\text{B}_1)$, and $\text{P}(^2\text{D}) + \text{H}_2(\text{X}^1\Sigma_g^+) \rightarrow \text{PH}(\text{X}^3\Sigma^-) + \text{H}(^2\text{S})$ is expected to become another typical case of the insertion reaction with a barrier.

The remaining part of this paper proceeds as follows. The details of *ab initio* calculation and CBS extrapolation are presented in Section 2. Section 3 expatiates each step for fitting the CHIPR PES of $\text{PH}_2(\text{X}^2\text{B}_1)$. The topographical features of the CHIPR PES are discussed in Section 4 and the QCT calculations are reported in Section 5. Finally, the concluding remarks are drawn in Section 6.

2 *Ab initio* calculations and CBS extrapolation

Ab initio energy points of the ground state $\text{PH}_2(\text{X}^2\text{B}_1)$ were obtained using the MOLPRO 2015 software package^{44,45} with the $C_s(\text{A}''')$ symmetry point group. The calculations were carried out as follows. Firstly, the single-configuration wavefunction of $\text{PH}_2(\text{X}^2\text{B}_1)$ was generated by the Hartree–Fock (HF) method. Then, the full-valence complete active space self-consistent field (CASSCF) method⁴⁶ was applied to obtain multi-configuration wavefunctions based on the HF wavefunction. In the CASSCF calculations, 11 active molecular orbitals ($9\text{A}' + 2\text{A}''$) and 5 closed core orbitals ($4\text{A}' + 1\text{A}''$) were considered. Finally, using the CASSCF wavefunctions as a reference, the dynamic correlation energies were computed by the internally contracted multireference configuration-interaction method including the Davidson correction [MRCI(Q)].^{47,48} During *ab initio* calculations, the Dunning-type basis sets^{49–51} aug-cc-pV(X + d)Z (X = T, Q) and aug-cc-pVXZ (X = T, Q) were selected for the P atom and H atom, respectively. For convenience, they are referred to as AVTdz and AVQdz, respectively.

A total of 12 339 *ab initio* energy points were distributed in two major structures of Jacobi coordinates. In the P–H₂ channel, the grids are defined by $1.4 \leq R_{\text{H–H}}/a_0 \leq 6$, $1.6 \leq r_{\text{P–HH}}/a_0 \leq 11.0$, and $0 \leq \gamma_{\text{P–HH}}/\text{deg} \leq 90^\circ$. In the H–PH channel, the ranges are defined by $1.6 \leq R_{\text{P–H}}/a_0 \leq 5$, $1.6 \leq r_{\text{H–PH}}/a_0 \leq 11.0$, and $0 \leq \gamma_{\text{H–PH}}/\text{deg} \leq 180^\circ$. Also, the grids in the vicinity of the equilibrium geometry and transition states were constructed to be dense enough. The MRCI(Q)/AVTdz and MRCI(Q)/AVQdz energies were used to extrapolate to the CBS limit. The complete active space (CAS) energies and dynamic correlation (dc) energies were extrapolated separately due to the distinct convergence rates, given by

$$E_X = E^{\text{CAS}} + E^{\text{dc}} \quad (1)$$

where the subscript *X* represents the basis set. The CAS energies were extrapolated using a two-point extrapolation protocol developed by Karton and Martin,⁵² *i.e.*,

$$E_X^{\text{CAS}} = E_{\infty}^{\text{CAS}} + B/X^{\lambda} \quad (2)$$

where $\lambda = 5.34$ is an effective decay parameter. While the dc energies were obtained using the Varandas uniform singlet- and triplet-pair extrapolation:⁵³

$$E_X^{\text{dc}}(R) = E_{\infty}^{\text{dc}}(R) + \frac{A_3}{(X + \beta)^3} + \frac{A_5}{(X + \beta)^5} \quad (3)$$

$$A_5 = A_5(0) + cA_3^{5/4} \quad (4)$$

where the predefined constants $A_5(0)$, c and β are chosen as $0.0037685459 E_h$, $-1.17847713 E_h^{-5/4}$ and $-3/8$, respectively.

3 The CHIPR potential energy surface

In the CHIPR method,^{33,36,37} the PES of a triatomic molecule assumes the MBE^{34,35} form:

$$V = \sum_{i=1}^3 V_{A_i}^{(1)} + \sum_{i \neq j}^3 V_{A_i A_j}^{(2)}(R_{ij}) + V_{A_1 A_2 A_3}^{(3)}(R_{12}, R_{13}, R_{23}) \quad (5)$$

where $V^{(1)}$ is the one-body fragment of each atom, $V^{(2)}$ is the two-body fragment in each dissociation scheme and $V^{(3)}$ is the three-body fragment. Generally, the zero of energy is chosen with all atoms far away from each other, and $V^{(1)}$ is non-zero only when the excitation of the atomic state exists in the dissociation scheme (see Section 3.1 for details).

Considering the permutational symmetry for an n -atom system, the CHIPR n -body term has the following form:^{36,37}

$$V^{(n)} = \sum_{i_1=0, \dots, i_{\tau}=0}^L C_{i_1, \dots, i_{\tau}} \hat{P} \left[\prod_{p=1}^{\tau} y_p^{i_p} \right] \quad (6)$$

where $C_{i_1, \dots, i_{\tau}}$ are expansion coefficients for a L th-order polynomial, \hat{P} is the operator which ensures the permutational symmetry, y_p are basis sets of coordinates ($p = 1, 2, \dots, \tau$) for the reference geometry and τ is the total number of internal degrees of freedom. y_p can be expanded by the distributed-origin contracted basis set:³³

$$y_p = \sum_{\alpha=1}^M c_{\alpha} \phi_{p,\alpha} \quad (7)$$

where c_{α} are the contraction coefficients, and α denotes each primitive function $\phi_{p,\alpha}$. The primitive function generally has one of the two following forms:³³

$$\phi_{p,\alpha} = \text{sech}^{\eta_{\alpha}}(\gamma_{p,\alpha} \rho_{p,\alpha}) \quad (8)$$

and

$$\phi_{p,\alpha} = \left[\frac{\tanh(\beta_{\alpha} R_p)}{R_p} \right]^{\sigma_{\alpha}} \text{sech}^{\eta_{\alpha}}(\gamma_{p,\alpha} \rho_{p,\alpha}) \quad (9)$$

where $\gamma_{p,\alpha}$ are non-linear parameters, $\rho_{p,\alpha} = R_p - R_{p,\alpha}^{\text{ref}}$ represents the deviation of the coordinate R_p from the primitive origin $R_{p,\alpha}^{\text{ref}}$, and the parameters η_{α} , σ_{α} and β_{α} are set to be values of 1, 6 and $1/5$,³³ respectively. It is worth noting that eqn (9) is used when the long-range terms are considered, otherwise, eqn (8) is

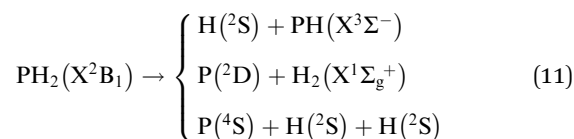
applied. The distributed origins $R_{p,\alpha}^{\text{ref}}$ are related by the following expression:³³

$$R_{p,\alpha}^{\text{ref}} = \zeta (R_p^{\text{ref}})^{\alpha-1} \quad (10)$$

where the parameters ζ and R_p^{ref} should be reasonably chosen during the fitting.

3.1 One-body fragment and switching function

According to the spin-spatial Wigner–Witmer correlation rules, the dissociation scheme of the ground state $\text{PH}_2(\text{X}^2\text{B}_1)$ can be described by



The diatomic molecules $\text{PH}(\text{X}^3\Sigma^-)$ and $\text{H}_2(\text{X}^1\Sigma_g^+)$ dissociate to their ground-state $\text{P}(\text{X}^4\text{S})$ and $\text{H}(\text{X}^2\text{S})$ atoms, while the excited-state $\text{P}(\text{X}^2\text{D})$ atom appears in the $\text{P}(\text{X}^2\text{D}) + \text{H}_2(\text{X}^1\Sigma_g^+)$ channel, as shown in Fig. 1. For an adiabatic PES of $\text{PH}_2(\text{X}^2\text{B}_1)$ dissociating to $\text{P}(\text{X}^4\text{S}) + \text{H}(\text{X}^2\text{S}) + \text{H}(\text{X}^2\text{S})$, it is necessary to construct a function to fulfill the smooth transformation between $\text{P}(\text{X}^2\text{D})$ and $\text{P}(\text{X}^4\text{S})$. Here, we adopted a switching function presented by Varandas.⁸ This function is widely used to model the correct transformation between excited- and ground-state atoms and to construct many PESs of triatomic molecules, such as $\text{NH}_2(\text{X}^2\text{B}_1)$,⁸ $\text{H}_2\text{S}^+(\text{X}^2\text{A}')$,¹² $\text{N}_2\text{O}(\text{X}^1\Sigma^+)$,⁶² etc. In this case, the one-body term can be written as

$$\sum_A V_A^{(1)} = V_{\text{P}(\text{X}^2\text{D})}^{(1)} f(R) = V_{\text{P}(\text{X}^2\text{D})}^{(1)} h(R_1) g(r_1) \quad (12)$$

where $V_{\text{P}(\text{X}^2\text{D})}^{(1)}$ is the excitation energy of $\text{P}(\text{X}^2\text{D})$, R_1 is the bond length of HH and r_1 is the distance between P and the center of

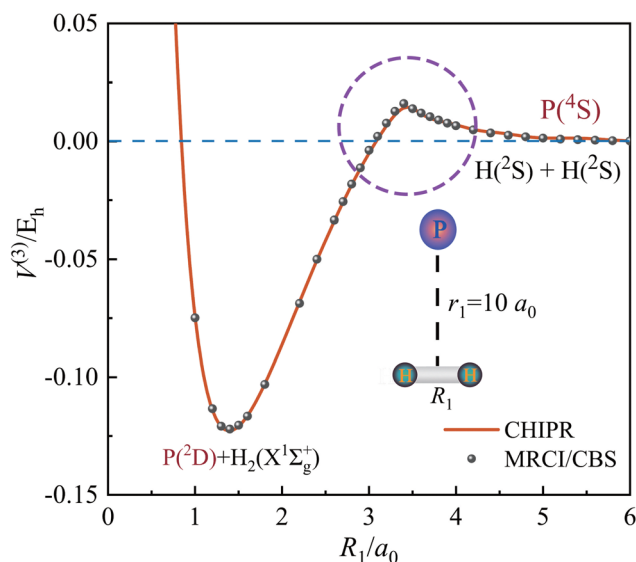


Fig. 1 The transition from $\text{P}(\text{X}^2\text{D})$ to $\text{P}(\text{X}^4\text{S})$ between the $\text{P}(\text{X}^2\text{D}) + \text{H}_2$ channel and the $\text{P}(\text{X}^4\text{S}) + \text{H} + \text{H}$ channel. The solid line is obtained from the CHIPR PES. Points are the CBS energies extrapolated by the MRCI(Q)/AVTZ and MRCI(Q)/AVQZ energies.

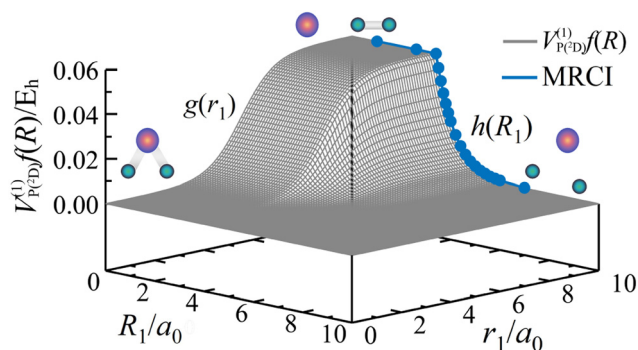


Fig. 2 The switching function for smoothing the CHIPR PES of the ground state $\text{PH}_2(\text{X}^2\text{B}_1)$.

mass of HH. $h(R_1)$ is used to adjust the transition from P^2D to P^4S between the $\text{P}^2\text{D} + \text{H}_2$ channel and the $\text{P}^4\text{S} + \text{H} + \text{H}$ channel, given by⁸

$$h(R_1) = \frac{1}{4} \sum_{i=1}^2 \left\{ 1 - \tanh \left[\alpha_i (R_1 - R_1^0) + \beta_i (R_1 - R_1^1)^3 \right] \right\} \quad (13)$$

where the parameters α_i , β_i , R_1^0 and R_1^1 ($i = 1, 2$) were obtained by the least-square fitting to 24 CBS energy points, *i.e.*, the blue points shown in Fig. 2. The CBS energies were extrapolated by the MRCI(Q)/AVTZ and MRCI(Q)/AVQZ energies. As shown in Fig. 1, $h(R_1)$ controls the decay from P^2D to P^4S with the increasing HH bond length, while keeping r_1 fixed at $10 a_0$. The amplitude function $g(r_1)$ is introduced in eqn (12) to annihilate $h(R_1)$ at short distances of r_1 (see Fig. 2), and thus to achieve a smooth and reliable PES, given by⁸

$$g(r_1) = \frac{1}{2} \{ 1 + \tanh [\alpha_0 (r_1 - r_1^0)] \} \quad (14)$$

where α_0 and r_1^0 are chosen to be 0.75 and 5.5, respectively, as suggested by Varandas.⁸ The calculated $V_{\text{P}^{(2)D}}^{(1)}$ is 11361.81 cm^{-1} , which agrees well with that of 11370.78 cm^{-1} obtained by summing over the weighted average energy of the $\text{P}^2\text{D}_{3/2}$ and $\text{P}^2\text{D}_{5/2}$ states (*i.e.* 11361.02 cm^{-1} and 11376.63 cm^{-1} , respectively) from the Atomic Spectra Database of National Institute of Standards and Technology.⁶³ It can be seen in Fig. 1 that there exists an avoid crossing located near $R_1 = 3.4 a_0$, which is well reproduced in this work. The parameters of switching function are collected in the ESI.†

3.2 Two-body fragment

In the CHIPR method, the two-body fragment is given in terms of eqn (6) by considering the Coulomb interaction, given by^{33,36}

$$V^{(2)}(R) = \frac{Z_A Z_B}{R} \sum_{k=1}^L C_k y^k \quad (15)$$

where Z_A and Z_B are the nuclear charges of the A and B atoms, respectively. According to eqn (5) and (11), the two-body fragments of the ground states $\text{H}_2(\text{X}^1\Sigma_g^+)$ and $\text{PH}(\text{X}^3\Sigma^-)$ are required. Their *ab initio* energy points were computed at the MRCI(Q)/aug-cc-pwCV5Z-DK level of theory. During the fitting,

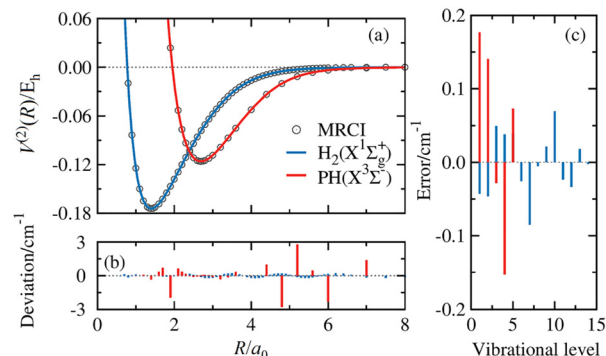


Fig. 3 (a) The PECs of $\text{PH}(\text{X}^3\Sigma^-)$ and $\text{H}_2(\text{X}^1\Sigma_g^+)$. Solid lines are the PECs fitted by the CHIPR form of eqn (6). Open circles are the *ab initio* energy points. (b) The deviations between *ab initio* energies and the corresponding energies from the unrefined CHIPR PECs. (c) The errors of vibrational level energies between previous measured values and those obtained from the experimentally-refined PECs.

M of the contracted bases in eqn (7) was chosen to be 4 and L of the polynomial expression in eqn (15) was chosen to be 8 for each two-body fragment. Fig. 3(a) shows the fitting CHIPR PECs of $\text{H}_2(\text{X}^1\Sigma_g^+)$ and $\text{PH}(\text{X}^3\Sigma^-)$, in which the root mean square deviation (RMSD) is 0.17 cm^{-1} and 0.93 cm^{-1} , respectively. Fig. 3(b) presents the deviations between *ab initio* energies and fitted energies, which are within $\pm 3 \text{ cm}^{-1}$. As shown, the obtained PECs of $\text{H}_2(\text{X}^1\Sigma_g^+)$ and $\text{PH}(\text{X}^3\Sigma^-)$ exhibit smooth and reasonable behaviors in both long and short internuclear ranges and the CHIPR method reproduces well with the *ab initio* results.

According to eqn (5), the three-body fragment will vanish as long as an atom moves away from the other two atoms. For the PES of $\text{PH}_2(\text{X}^2\text{B}_1)$, the configurations of P-H_2 and H-PH depend greatly on the two-body fragments. Also, the diatomic molecule acts as the reactant or product and the high-precision two-body fragments can correctly reproduce the initial and final states of the reaction. Therefore, we used the experimental spectroscopic constants,^{55,57–59} including equilibrium geometries, dissociation energies, vibrational frequencies (in Table 1) and the energies of vibrational levels ν (in Table 2) to refine the PECs of $\text{H}_2(\text{X}^1\Sigma_g^+)$ and $\text{PH}(\text{X}^3\Sigma^-)$. A total of 14 measured vibrational levels for $\text{H}_2(\text{X}^1\Sigma_g^+)$ ⁵⁹ and 5 measured vibrational levels for $\text{PH}(\text{X}^3\Sigma^-)$ ⁵⁷ were adopted during the refining process. The refining process was carried out in the CHIPR 4.0 program³⁷ and the LEVEL program⁶⁴ was used to calculate the vibrational level energies of our PECs. The spectroscopic constants and vibrational level energies of the refined $\text{H}_2(\text{X}^1\Sigma_g^+)$ and $\text{PH}(\text{X}^3\Sigma^-)$ PECs are also listed in Tables 1 and 2, respectively. Fig. 3(c) prints the errors between our refined vibrational level energies and the measured values, which are within $\pm 0.2 \text{ cm}^{-1}$. The refined vibrational level energies also agree well with those calculated by Roueff *et al.*⁶⁰ and Langleben *et al.*,⁶¹ whose data are included in the Strasbourg astronomical Data Center.⁶⁵ Hence, the two-body fragments of our CHIPR PES for $\text{H}_2(\text{X}^1\Sigma_g^+)$ and $\text{PH}(\text{X}^3\Sigma^-)$ are accurate and reliable. The coefficients of the refined $\text{H}_2(\text{X}^1\Sigma_g^+)$ and $\text{PH}(\text{X}^3\Sigma^-)$ PECs are displayed in the ESI.†

Table 1 The spectroscopic constants of the CHIPR two-body fragments, along with previous theoretical and experimental results

Method	R_e^a	D_e^b	ω_e^c	$\omega_e x_e^c$	α_e^c	B_e^c
$H_2(X^1\Sigma_g^+)$						
CHIPR ^d	1.401	4.743	4420.56	125.27	3.396	62.926
CHIPR ^e	1.401	4.748	4405.26	120.19	2.945	60.792
Theory ^f	1.401	4.711	4389.66	121.56	3.162	60.826
Exp. ^g	1.401	4.748	4401.21	121.33	3.062	60.853
$PH(X^3\Sigma^-)$						
CHIPR ^d	2.693	3.155	2367.01	44.151	0.254	8.517
CHIPR ^e	2.686	3.187	2365.10	44.08	0.256	8.553
Theory ^h	2.683	3.18	2392.51	47.5	0.253	8.534
Exp. ⁱ	2.687 ⁱ	3.18 ^j	2363.77 ⁱ	43.91 ⁱ	0.253 ⁱ	8.539 ⁱ

^a The equilibrium geometry, a_0 . ^b The dissociation energy, eV. ^c The units of ω_e , $\omega_e x_e$, α_e and B_e are cm^{-1} . ^d The CHIPR PECs fitted by the *ab initio* energies. ^e The experimentally-refined CHIPR PECs *via* multi-property fit to the experimental spectroscopic constants. ^f Results at the MRCI/AV6Z level from Ynag *et al.*⁵⁴ ^g Ref. 55. ^h Results at the MRCI(Q)/AV5Z level from Gao *et al.*⁵⁶ ⁱ Results obtained by Fourier transform infrared emission spectroscopy from Ram and Bernath.⁵⁷ ^j Ref. 58.

Table 2 The energies (cm^{-1}) of vibrational levels (v) for the refined CHIPR two-body fragments, along with previous theoretical and experimental results

v	$H_2(X^1\Sigma_g^+)$			$PH(X^3\Sigma^-)$		
	Exp. ^a	Theory ^b	CHIPR ^c	Exp. ^d	Theory ^e	CHIPR ^c
1	4161.14	4161.16	4161.18	2276.21	2276.21	2276.03
2	8086.93	8087.00	8086.98	4465.02	4465.01	4464.88
3	11782.36	11782.39	11782.31	6566.16	6566.16	6566.18
4	15250.31	15250.37	15250.27	8578.94	8578.95	8579.10
5	18491.92	18491.93	18491.88	10502.19	10502.20	10502.12
6	21505.78	21505.78	21505.81			12332.99
7	24287.91	24287.92	24288.00			14068.44
8	26831.16	26831.09	26831.17			15704.03
9	29124.09	29124.04	29124.07			17233.84
10	31150.47	31150.39	31150.40			18650.16
11	32887.13	32887.10	32887.15			19943.10
12	34302.20	34302.17	34302.23			21100.12
13	35351.36	35351.31	35351.34			22105.55
14	35973.38	35973.27	35973.38			22940.59

^a Results obtained by flash discharge spectra from Dabrowski.⁵⁹

^b Results obtained by nonadiabatic perturbation theory from Roueff *et al.*⁶⁰

^c Results obtained from the experimentally-refined CHIPR PECs. ^d Results obtained by Fourier transform infrared emission spectroscopy from Ram and Bernath.⁵⁷ ^e Results at the MRCI(Q)/AV5Z level from Langleben *et al.*⁶¹

3.3 Three-body fragment

Once the switching function and two-body fragments are determined, the three-body energies $\varepsilon^{(3)}(\mathbf{R})$ can be obtained by

$$\varepsilon^{(3)}(\mathbf{R}) = E(\mathbf{R}) - \sum_{i=1}^3 V_i^{(2)}(R_i) - V_{P(2D)}^{(1)} h(R_1) g(r_1) \quad (16)$$

where $E(\mathbf{R})$ is the relative energy of a triatomic molecule, *i.e.*, the CBS energy relative of $PH_2(X^2B_1)$ to its $P(^4P) + H(^2S) + H(^2S)$ asymptote. In the CHIPR method, the three-body fragment has the following form:³⁶

$$V^{(3)}(\mathbf{R}) = \sum_{i,j,k=0}^L C_{i,j,k} \left\{ \sum_g^{g \leq G} P_g^{(i,j,k)} [y_1^i y_2^j y_3^k] \right\} \quad (17)$$

Table 3 Stratified root-mean-square deviations (RMSDs) of the CHIPR PES

Energy ^a	N^b	Max deviation ^c	RMSD ^c	$N^d_{>\text{RMSD}}$
10	2765	153.9	32.3	706
20	3221	192.2	34.1	736
30	3627	198.0	36.3	703
40	4011	198.0	37.1	766
50	4488	198.0	38.1	825
60	5048	198.0	38.2	950
70	5903	198.0	37.1	1129
80	7051	198.0	35.9	1353
90	8320	252.3	36.5	1632
100	8910	252.3	36.8	1781
150	10 907	266.2	41.3	2149
200	11 447	266.2	42.1	2335
800	12 247	266.2	41.8	2481
1700	12 339	266.2	41.7	2493

^a The energy range, kcal mol^{-1} . ^b The number of energy points in the corresponding range. ^c The units of maximum deviation and RMSD are cm^{-1} . ^d The number of energy points with a deviation larger than the RMSD.

where $C_{i,j,k}$ are expansion coefficients. Also, $C_{i,j,k}$ should satisfy the general constraints, *i.e.*, $i+j+k \neq i \neq j \neq k$ and $i+j+k \leq L$ (see Rochas work for details³⁶). To avoid unphysical holes at high-energy interaction regions, eqn (17) is multiplied by a damp function:^{33,37}

$$D^{(3)}(\mathbf{R}) = \left[\frac{1}{8} \prod_{i=1}^3 \{1 + \tanh[\kappa(R_i - R_0)]\} \right]^\xi \quad (18)$$

where $R_0 = 0.6 a_0$, $\kappa = 30 a_0^{-1}$ and $\xi = 10$. This damp function ensures that the three-body fragment gradually disappears as the configuration approaches the high-energy interaction regions.

During the fitting of the three-body fragment, M of the contracted bases in eqn (7) was chosen to be 4 and L of the polynomial expression in eqn (17) was chosen to be 14. Table 3 lists the accumulated RMSD with respect to the ascending ordered CBS energies. A total of 12 339 CBS energies was utilized in the nonlinear least-square fitting procedure, covering an energy range up to about 1700 kcal mol^{-1} above the global minimum of $PH_2(X^2B_1)$. As expected, the CHIPR PES reproduces the *ab initio* energy points well near the equilibrium geometry of $PH_2(X^2B_1)$. For the remaining configurations, it also provides a surprising fitting accuracy, especially for the high-energy points. The results show a high fitting accuracy with a total RMSD of 41.7 cm^{-1} (or 0.119 kcal mol^{-1}). The coefficients of the three-body fragment are displayed in the ESI.†

4 Features of CHIPR PES

Topographical features of the CHIPR PES for the ground state $PH_2(X^2B_1)$ are shown in Fig. 4 and 5, which display the important stationary points, namely the global minimum (GM), transition state (TS), second-order saddle (SP) and local minimum (MIN). Table 4 presents the main attributes of the stationary points on the CHIPR PES, including the potential energies (E) relative to the $P(^4S) + H(^2S) + H(^2S)$ asymptote, the interatomic distances for HH (R_1) and PH (R_2 and R_3), the HPH

bond angle (θ), the dissociation energy $D_0(\text{HP-H})$ and the vibration frequencies, including the symmetrical stretching ω_1 , bending ω_2 and antisymmetric stretching ω_3 . Table 4 also collects the geometry optimization (OPTG)⁶⁶ results for GM, TS1 and TS2 as implemented in MOLPRO 2015.^{44,45}

Fig. 4(a) presents the contour map of $\text{PH}_2(\text{X}^2\text{B}_1)$ for the PH bond stretching in the HPH bending configuration with θ fixed at 92.09° . It can be seen that the GM of the C_{2v} symmetry locates at $R_1 = 3.860 a_0$ and $R_2 = R_3 = 2.681 a_0$, which are also given in Fig. 4(d) and 5(b). The corresponding dissociation energy $D_0(\text{HP-H})$ is computed to be $77.435 \text{ kcal mol}^{-1}$ and the vibrational frequencies are 2385 cm^{-1} , 1072.83 cm^{-1} and 2395.69 cm^{-1} for ω_1 , ω_2 and ω_3 , respectively. As shown in Table 4, the attributes of GM are very similar to those from our OPTG at the MRCI(Q)/AV6Z level and those from the previous theoretical results calculated at the CISD/VQZ level²⁸ and RECP/MRSDCI level.³⁰ The attributes also agree well with the measured ones shown in Table 4, but the ω_1 values from all of the four theoretical studies are about 100 cm^{-1} larger than that of the measurement.¹⁷ Although the P atom could possibly be better simulated using

the ECP10MWB basis set,⁶⁷ no attempt has been made due to the unaffordable computational costs.

Fig. 4(b) and (c) display the contour plots for bond stretching in the HPH and PHH collinear configurations, respectively. As shown in Fig. 4(b), a transition state (TS1) is found to locate at $R_1 = 5.228 a_0$ and $R_2 = R_3 = 2.614 a_0$ with $D_{\infty h}$ symmetry, connected with the symmetrically distributed second-order saddle points (SP1). The stationary points TS1 and SP1 are associated to the linear $^2\Pi$ structure of PH_2 where the X^2B_1 and A^2A_1 Renner–Teller states become degenerate. As shown in Table 4, the attributes of TS1 are similar to those from our OPTG at the MRCI(Q)/AV6Z level and those calculated by Kayi *et al.*²⁹ at the CASSCF/AVTZ level. Fig. 4(d) shows the contour plot for the C_{2v} insertion of the P atom into the H_2 fragment, which exhibits GM, TS1 and another transition state (TS2) of C_{2v} symmetry. The transition state TS2 is found to be located at $R_1 = 1.413 a_0$ and $R_2 = R_3 = 4.992 a_0$, which has a profound effect on the insertion reaction of $\text{P}(^2\text{D}) + \text{H}_2(\text{X}^1\Sigma_g^+)$. Hence, the OPTG were carried out for TS2 at the MRCI(Q)/AV5dZ and MRCI(Q)/AVQdZ level to validate the attributes of TS2 on our fitted CHIPR PES, which shows an excellent agreement.

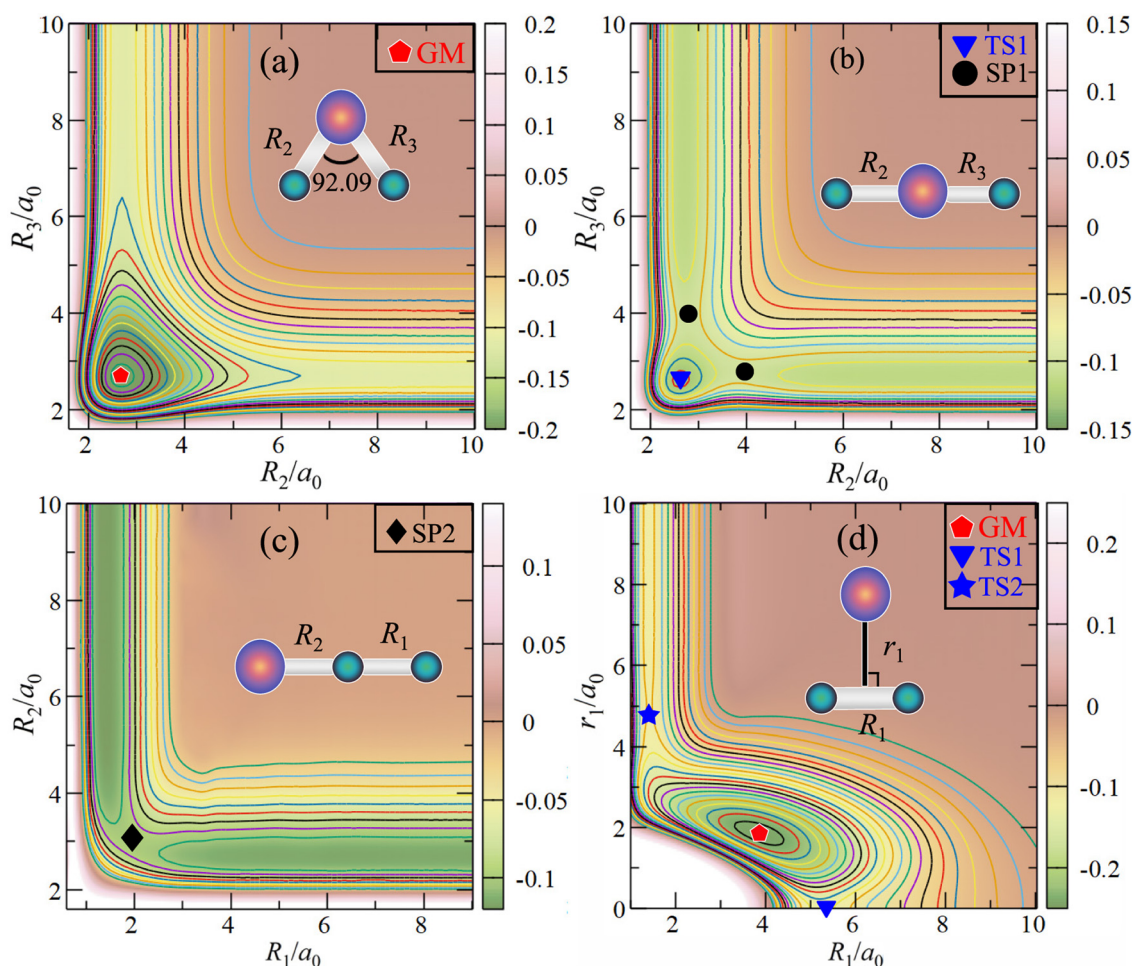


Fig. 4 (a) The contour plot for bond stretching in the HPH bending configuration with θ fixed at 92.09° . (b) The contour plot for bond stretching in the HPH collinear configuration. (c) The contour plot for bond stretching in the PHH collinear configuration. (d) The contour plot for the C_{2v} insertion of the P atom into the H_2 fragment. Contours are equally spaced by $0.01 E_h$, starting from $-0.24 E_h$ for panels (a) and (d), $-0.13 E_h$ for panel (b), and $-0.105 E_h$ for panel (c).

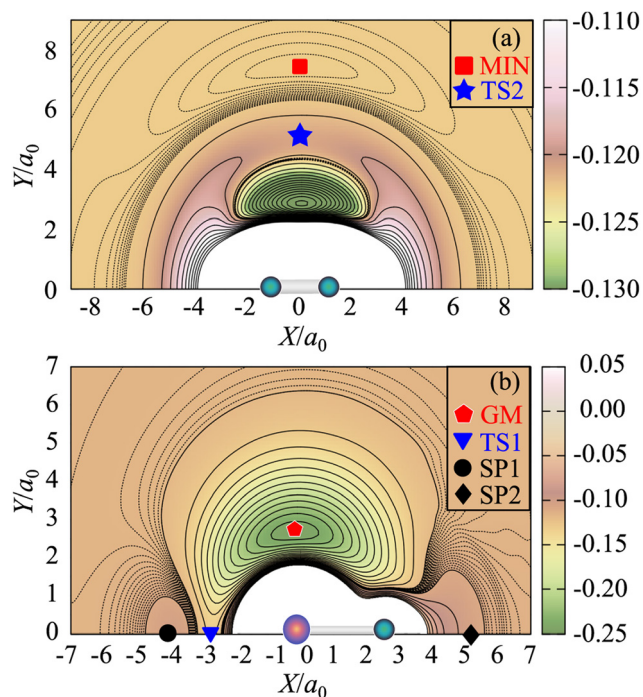


Fig. 5 (a) The contour plot for P moving around H_2 with R_1 fixed at $1.401 a_0$. Contours are equally spaced by $0.002 E_h$, starting at $-0.15 E_h$. Dashed areas are contours equally spaced by $0.000025 E_h$, starting at $-0.1229 E_h$. (b) The contour plot for H moving around PH with R_2 fixed at $2.681 a_0$. Contours are equally spaced by $0.01 E_h$, starting at $-0.24 E_h$. Dashed areas are contours equally spaced by $0.0005 E_h$, starting at $-0.12 E_h$.

Fig. 5 illustrates the long-range behavior of the CHIPR PES, so as to provide a reliable description of the van der Waals configuration and the associated transition state. The brown band shown in Fig. 5(a) reveals that a barrier exists in the entrance channel of the $P(^2D) + H_2(X^1\Sigma_g^+)$ system for all interatomic orientations and its weakest configuration is TS2. It also shows a van der Waals minimum (the MIN in Table 4) of C_{2v} symmetry, which connects TS2 and the $P(^2D) + H_2(X^1\Sigma_g^+)$ dissociation limit. This connecting path demonstrates that the insertion of the P atom along the mid-perpendicular of the HH bond is relatively easy to cross the barrier around H_2 , resulting in the relevant reaction. On the contrary, Fig. 5(b) implies that the $H(^2S) + PH(X^3\Sigma^-)$ reaction is a barrierless insertion reaction for most interatomic orientations.

To better view the major topographical features, a relaxed triangular contour plot⁶⁸ for the CHIPR PES is displayed in Fig. 6 based on the scaled hyperspherical coordinates ($\beta^* = \beta/Q$ and $\gamma^* = \gamma/Q$), given by

$$\begin{pmatrix} Q \\ \beta \\ \gamma \end{pmatrix} = \begin{pmatrix} 1 & 1 & 1 \\ 0 & \sqrt{3} & -\sqrt{3} \\ 2 & -1 & -1 \end{pmatrix} \begin{pmatrix} R_1^2 \\ R_2^2 \\ R_3^2 \end{pmatrix} \quad (19)$$

As shown in Fig. 6, the locations and symmetries of all stationary points for the ground-state $PH_2(X^2B_1)$ are illustrated explicitly. The CHIPR PES of the ground-state $PH_2(X^2B_1)$ exhibits a smooth and reasonable behavior. The critical equilibrium

Table 4 Attributes for the stationary points of the $PH_2(X^2B_1)$ CHIPR PES

	Method	E/E_h	R_1/a_0	R_2/a_0	R_3/a_0	θ/deg	ω_1/cm^{-1}	ω_2/cm^{-1}	ω_3/cm^{-1}	D_0^a (HP-H)
Global minimum										
GM(C_{2v})	CHIPR	-0.2460	3.860	2.681	2.681	92.09	2385	1084.09	2395.69	77.435
	AV6Z ^b	-0.2469	3.857	2.679	2.679	92.08	2386.11	1121.51	2394.67	78.000
	Theory ^c		3.856	2.683	2.683	91.87	2396	1125	2404	
	Theory ^d		3.842	2.680	2.680	91.6				72.2
	Exp.		3.846 ^e	2.680 ^e	2.680 ^e	91.7 ^e	2295 \pm 15 ^f	1101.98 ^g		
	Exp.		3.865 ^h	2.698 ^h	2.698 ^h	91.49 ^h	2298 \pm 3 ⁱ	1102 \pm 3 ⁱ		74.2 \pm 2 ^j
Transition state										
TS1($D_{\infty h}$)	CHIPR	-0.1335	5.228	2.614	2.614	180	2392.92	1682.69i	2726.93	
	AV6Z ^b	-0.1320	5.252	2.626	2.626	180	2484.57	1679.11i	2629.4	
	Theory ^k		5.254	2.627	2.627	180		1770i		
TS2(C_{2v})	CHIPR	-0.1211	1.413	4.992	4.992	16.27	4288.97	300.97i	549.96	
	AV5dZ ^b	-0.1213	1.415	4.914	4.914	16.56	4344.05	176.01i	578.09	
	AVQdZ ^b	-0.1205	1.416	4.902	4.902	16.61	4275.53	325.04i	402.21	
Second-order saddle										
SP1($C_{\infty v}$)	CHIPR	-0.1047	6.610	2.762	3.848	180	945.04i	1998.62	1060.13i	
SP2($C_{\infty v}$)	CHIPR	-0.1008	1.951	2.998	4.948	0	1161.09	931.93i	1458.28i	
Local minimum										
MIN(C_{2v})	CHIPR	-0.1229	1.390	7.450	7.450	10.71	4397.04	36.01	65.76	

^a The unit of D_0 (HP-H) is kcal mol⁻¹. ^b Results from the geometry optimization. ^c Results at the CISD/VQZ level from Woodcock *et al.*²⁸ ^d Results at the RECP/MRSDCI level from Balasubramanian *et al.*³⁰ ^e Equilibrium geometry deduced from the rotational constants of the 000-000 band.²⁰ ^f Vibrational frequency obtained by the 1 \leftarrow 0 transition of the symmetric stretch from photoelectron spectroscopy.¹⁹ ^g Origin of the bending fundamental band obtained from the laser magnetic resonance spectrum.¹⁶ ^h Equilibrium geometry deduced from the rotational constants of 0₀⁰, 2₁¹ and 2₁¹ ($n = 1-3$) bands.²² ⁱ Term values of the (100) and (010) vibrational levels from dispersed fluorescence spectroscopy.¹⁷ ^j The result obtained from the photoionization mass spectrometric study.²⁴ ^k Results at the CASSCF/AVTZ level from Kayi *et al.*²⁹

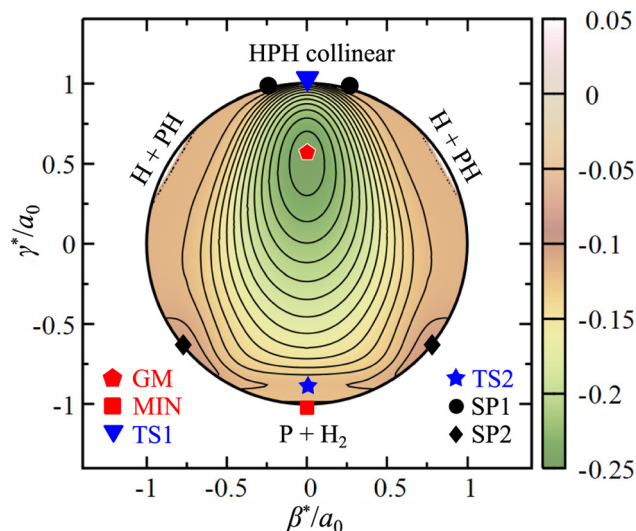


Fig. 6 The relaxed triangular contour plot for the ground-state PH_2 in hyperspherical coordinates. Contours are equally spaced by $0.01 E_h$, starting at $-0.24 E_h$.

geometry and transition states are well reproduced. Hence, this CHIPR PES is reliable for the dynamic calculations.

5 Dynamic calculations

Based on our CHIPR PES of $\text{PH}_2(\text{X}^2\text{B}_1)$, the dynamic calculations of the $\text{P}(\text{D}) + \text{H}_2(\text{X}^1\Sigma_g^+) \rightarrow \text{PH}(\text{X}^3\Sigma^-) + \text{H}(\text{S})$ reaction were carried out with the QCT method.^{42,43} The integration of the classical equations of motion employs a time step of 0.2 fs. For each case, a total of 10 000 trajectories were sampled and the initial distance of the reactants was 15 Å. The integral cross section (ICS) of $\text{P} + \text{H}_2(\nu, j) \rightarrow \text{PH} + \text{H}$ was calculated by⁴³

$$\sigma_r(E_{\text{tr}}; \nu, j) = \pi b_{\text{max}}^2 \frac{N_r}{N} \quad (20)$$

where N is the total number of sampled trajectories, N_r is the number of reactive trajectories and b_{max} is the maximum impact parameter determined in the traditional way.⁴² The thermal rate constant was obtained by averaging the internal states of the reactant and translational energy.⁴³

$$k(T) = g_e(T) \left(\frac{2}{k_B T} \right)^{3/2} \left(\frac{1}{\pi} \right)^{1/2} Q_{\nu j}^{-1}(T) \sum_{\nu j} (2j+1) \times \exp\left(-\frac{E_{\nu j}}{k_B T}\right) \int_0^\infty E_{\text{tr}} \sigma^x \exp\left(-\frac{E_{\text{tr}}}{k_B T}\right) dE_{\text{tr}} \quad (21)$$

where $Q_{\nu j}(T)$ is the rovibrational partition function for all the states of $\text{H}_2(\text{X}^1\Sigma_g^+)$, $E_{\nu j}$ is the (ν, j) state energy, E_{tr} is the translation energy, k_B is the Boltzmann constant and $g_e(T)$ is the electronic degeneracy factor. The dynamic calculation was performed adiabatically on the ground state $\text{PH}_2(\text{X}^2\text{B}_1)$ and the $g_e(T)$ assumed the form:⁶⁹

$$g_e(T) = g_{\text{PH}_2}(T)(q_{\text{P}}(T)q_{\text{H}_2}(T))^{-1} \quad (22)$$

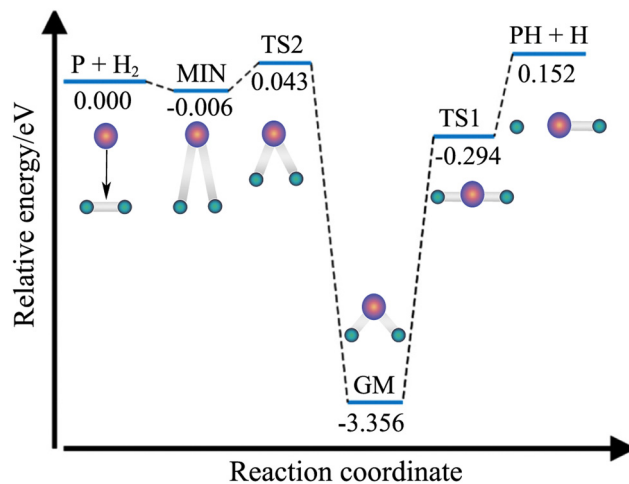


Fig. 7 The energy diagram for the reaction pathway and relative stationary points of $\text{P}(\text{D}) + \text{H}_2(\text{X}^1\Sigma_g^+) \rightarrow \text{PH}(\text{X}^3\Sigma^-) + \text{H}(\text{S})$. Energies are given relative to the $\text{P}(\text{D}) + \text{H}_2(\text{X}^1\Sigma_g^+)$ asymptote with the unit of eV.

where $g_{\text{PH}_2}(T) = 2$ is the degeneracy of the ground state $\text{PH}_2(\text{X}^2\text{B}_1)$, $q_{\text{H}_2}(T) = 1$ is the electronic partition functions accounting for the fine structure of $\text{H}_2(\text{X}^1\Sigma_g^+)$ and $q_{\text{P}}(T)$ is the electronic partition function accounting for the fine structure of $\text{P}(\text{D})$, given by

$$q_{\text{P}}(T) = 4 + 6 \exp(-22.46/T) \quad (23)$$

Fig. 7 displays the most likely minimum energy path for the $\text{P}(\text{D}) + \text{H}_2(\text{X}^1\Sigma_g^+) \rightarrow \text{PH}(\text{X}^3\Sigma^-) + \text{H}(\text{S})$ reaction and the energies of relative stationary points on the CHIPR PES. As stated in Section 4, the insertion of the P atom may well approach along the mid-perpendicular of H_2 , so as to cross the surrounding barrier more easily. In this process, the van der Waals configuration MIN is transiently formed, followed by an unstable transition state TS2. Subsequently, θ opens progressively and R_1 increases simultaneously, then evolves through GM and the linear transition state TS1, as shown in the Fig. 4(d). Finally, the linear PH_2 dissociates to the products of $\text{PH}(\text{X}^3\Sigma^-)$ and $\text{H}(\text{S})$.

The ICSs for the $\text{P}(\text{D}) + \text{H}_2(\text{X}^1\Sigma_g^+; \nu = 0-4, j = 0) \rightarrow \text{PH}(\text{X}^3\Sigma^-) + \text{H}(\text{S})$ reactions as a function of the collision energy are displayed in Fig. 8. The results show that the ICS rises rapidly for the low collision energy and then gradually reaches a stabilization at the high collision energy. Also, there is a threshold for the ICS of the $\text{P}(\text{D}) + \text{H}_2(\text{X}^1\Sigma_g^+) \rightarrow \text{PH}(\text{X}^3\Sigma^-) + \text{H}(\text{S})$ reaction due to the C_{2v} barrier (TS2) on its insertion reaction path. The calculated ICS of $\text{P}(\text{D}) + \text{H}_2(\text{X}^1\Sigma_g^+; \nu = 0, j = 0)$ is 0.342 Å^2 with a collision energy of 0.05 eV, so the effective threshold is expected to be slightly less than 0.05 eV, which is similar to that of the corresponding C_{2v} barrier energy, i.e., 0.043 eV relative to the $\text{P}(\text{D}) + \text{H}_2(\text{X}^1\Sigma_g^+)$ limit. Meanwhile, the vibrational excitation of the reactant has a significant effect on its reactivity. Predictably, the threshold tends to decrease for the increasing vibrational excitations. In other words, the increase of vibrational energy may meet the need for the reaction through the path with a barrier, resulting in the lower demand of the collision energy for high vibrational states.

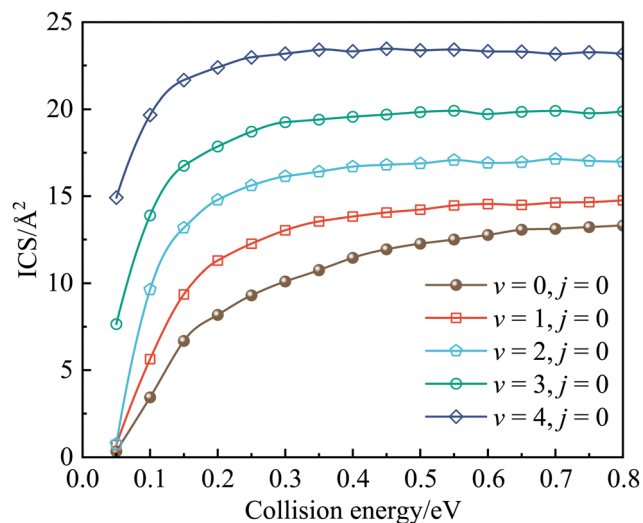


Fig. 8 The integral cross section for the $P(^2D) + H_2(X^1\Sigma_g^+; v = 0-4, j = 0)$ reactions as a function of the collision energy.

Fig. 9 presents the thermal rate constant for $P(^2D) + H_2(X^1\Sigma_g^+) \rightarrow PH(X^3\Sigma^-) + H(^2S)$ from 150 to 5000 K. This reaction is endothermic and characterized by an activation barrier, which is slow at low temperatures. Also, the rate constant follows an Arrhenius-type temperature dependence at relatively low temperature, as shown in the inset of Fig. 9. At high temperature, however, the effect of the barrier is weakened and the activation energy of the reaction becomes temperature-dependent. Then, we fitted the calculated rate constant using the three-parameter Kooij function,⁷⁰ given by

$$k(T) = A \left(\frac{T}{300} \right)^m e^{-\beta_k/T} \quad (24)$$

where the parameters A , m and β_k are $3.02196 \times 10^{-11} \text{ cm}^3 \text{ s}^{-1}$, 0.74105 and 616.25007 K, respectively. The fitted $k(T)$ deviates less than 4 per cent from our calculated ones.

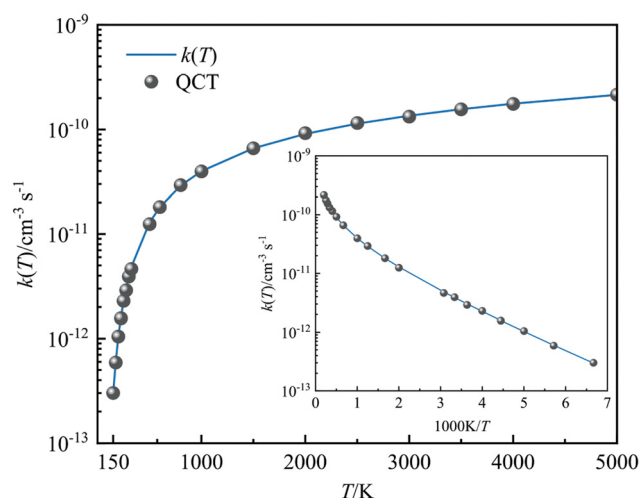


Fig. 9 The thermal rate constant for the $P(^2D) + H_2(X^1\Sigma_g^+) \rightarrow PH(X^3\Sigma^-) + H(^2S)$ reaction from 150 to 5000 K.

6 Conclusions

In this work, we have constructed an accurate and global PES for the electronic ground state of $PH_2(X^2B_1)$. A total of 12 339 *ab initio* energy points for $PH_2(X^2B_1)$ are computed at the MRCI(Q) level with the AVTdZ and AVQdZ basis sets, which are then extrapolated to the CBS limit. The CHIPR method is used to construct the global PES for $PH_2(X^2B_1)$. Thereinto, a switching function is constructed to model the transition between $P(^2D)$ and $P(^4S)$. The *ab initio* potential energy curves of $H_2(X^1\Sigma_g^+)$ and $PH(X^3\Sigma^-)$ are also calculated and then refined by various experimental spectroscopic constants, including equilibrium geometries, dissociation energies, vibrational frequencies and vibrational level energies. The RMSD of the CHIPR PES is only 41.7 cm^{-1} . The topographical features of the present PES are smooth and reasonable. The geometries and vibrational frequencies of the main stationary points agree well with the available experimental and theoretical results.

Based on the CHIPR PES of $PH_2(X^2B_1)$, we have carried out the QCT calculations for the $P(^2D) + H_2(X^1\Sigma_g^+) \rightarrow PH(X^3\Sigma^-) + H(^2S)$ reaction. The ICSs for the reactions are obtained as a function of the collision energy. The results show a typical characteristic of a barrier reaction and the reactivity is sensitive to the vibrational excitation. Meanwhile, the thermal rate constant for the $P(^2D) + H_2(X^1\Sigma_g^+) \rightarrow PH(X^3\Sigma^-) + H(^2S)$ reaction is predicted as a function of temperature and fitted by the Arrhenius-Kooij function. The computed cross sections and rate constants may be used to investigate the chemical evolution of the P atom in astrophysical environments such as Saturn and Jupiter.

Conflicts of interest

There are no conflicts to declare.

Acknowledgements

This work is supported by the National Natural Science Foundation of China (Grant no. 52106098 and 11604179) and the Natural Science Foundation of Shandong Province (Grant no. ZR2021QE021 and ZR2016AQ18). Zhi Qin also acknowledges the support from the China Postdoctoral Science Foundation (2021M701977), the Postdoctoral Innovation Project of Shandong Province and the Postdoctoral Applied Research Project of Qingdao City. The scientific calculations in this paper have been done on the HPC Cloud Platform of Shandong University.

Notes and references

- 1 R. Courtin, D. Gautier, A. Marten, B. Bézard and R. Hanel, *Astrophys. J.*, 1984, **287**, 899–916.
- 2 A. Tokunaga, S. Ridgway, L. Wallace and R. Knacke, *Astrophys. J.*, 1979, **232**, 603–615.
- 3 M. Agúndez, J. Cernicharo, L. Decin, P. Encrenaz and D. Teyssier, *Astrophys. J., Lett.*, 2014, **790**, L27.

- 4 D. Baugh, B. Koplitz, Z. Xu and C. Wittig, *J. Chem. Phys.*, 1988, **88**, 879–887.
- 5 R. Prinn and J. Lewis, *Bull. Am. Astron. Soc.*, 1975, 381.
- 6 J. Lee, J. Michael, W. Payne, D. Whytock and L. Stief, *J. Chem. Phys.*, 1976, **65**, 3280–3283.
- 7 B. Bussery-Honvault, v Honvault and J.-M. Launay, *J. Chem. Phys.*, 2001, **115**, 10701–10708.
- 8 A. Varandas and L. Poveda, *Theor. Chem. Acc.*, 2006, **116**, 404–419.
- 9 L. Peng, H. Ma, Y. Lü, C. Zhang, S. Gao, S. Liu and Y. Li, *Mol. Phys.*, 2021, **119**, e1928313.
- 10 E. J. Rackham, T. Gonzalez-Lezana and D. E. Manolopoulos, *J. Chem. Phys.*, 2003, **119**, 12895–12907.
- 11 S. Chai, H. Wang, Y. Lü, Q. Guo and Y. Li, *Phys. Chem. Chem. Phys.*, 2020, **22**, 26544–26551.
- 12 L. Zhang, S. Gao, Q. Meng, J. Pan and Y. Song, *J. Chem. Phys.*, 2018, **149**, 154303.
- 13 H. Guo, *Int. Rev. Phys. Chem.*, 2012, **31**, 1–68.
- 14 F. Aoiz, L. Bañares and V. Herrero, *J. Phys. Chem. A*, 2006, **110**, 12546–12565.
- 15 D. Ramsay, *Nature*, 1956, **178**, 374–375.
- 16 G. Hills and A. McKellar, *J. Chem. Phys.*, 1979, **71**, 1141–1149.
- 17 Z. Jakubek, P. Bunker, M. Zachwieja, S. Nakhate, B. Simard, S. Yurchenko, W. Thiel and P. Jensen, *J. Chem. Phys.*, 2006, **124**, 094306.
- 18 P. Zittel and W. Lineberger, *J. Chem. Phys.*, 1976, **65**, 1236–1243.
- 19 K. M. Ervin and W. C. Lineberger, *J. Chem. Phys.*, 2005, **122**, 194303.
- 20 J.-M. Berthou, B. Pascat, H. Guenebaut and D. Ramsay, *Can. J. Phys.*, 1972, **50**, 2265–2276.
- 21 Y. Chen, Q. Zhang, D. Zhang, C. Chen, S. Yu and X. Ma, *Chem. Phys. Lett.*, 1994, **223**, 104–109.
- 22 D.-f Zhao, C.-b Qin, Q. Zhang and Y. Chen, *Chin. J. Chem. Phys.*, 2011, **24**, 8.
- 23 T. Hirao, S.-i Hayakashi, S. Yamamoto and S. Saito, *J. Mol. Spectrosc.*, 1998, **187**, 153–162.
- 24 J. Berkowitz, L. Curtiss, S. Gibson, J. Greene, G. Hillhouse and J. Pople, *J. Chem. Phys.*, 1986, **84**, 375–384.
- 25 J.-P. Gu, M.-B. Huang, F. Kong and S.-H. Liu, *J. Mol. Struct.*, 1989, **201**, 39–47.
- 26 K. Balasubramanian, *Chem. Phys. Lett.*, 1993, **204**, 601–607.
- 27 C. Puzzarini and V. Barone, *J. Chem. Phys.*, 2010, **133**, 184301.
- 28 H. L. Woodcock, S. S. Wesolowski, Y. Yamaguchi and H. F. Schaefer, *J. Phys. Chem. A*, 2001, **105**, 5037–5045.
- 29 H. Kayi, I. B. Bersuker and J. E. Boggs, *J. Mol. Struct.*, 2012, **1023**, 108–114.
- 30 K. Balasubramanian, Y. S. Chung and W. S. Glaunsinger, *J. Chem. Phys.*, 1993, **98**, 8859–8869.
- 31 S. Yurchenko, W. Thiel, P. Jensen and P. Bunker, *J. Mol. Spectrosc.*, 2006, **239**, 160–173.
- 32 D. Zhang, Q. Tang, J. Zhang, S. Deheng and Y. Benhai, *Acta Phys. Sin.*, 2009, **58**, 5323–5328.
- 33 A. Varandas, *J. Chem. Phys.*, 2013, **138**, 054120.
- 34 A. J. Varandas and J. N. Murrell, *Faraday Discuss. Chem. Soc.*, 1977, **62**, 92–109.
- 35 J. N. Murrell, *Molecular potential energy functions*, J. Wiley, 1984.
- 36 C. M. Rocha and A. J. Varandas, *Comput. Phys. Commun.*, 2020, **247**, 106913.
- 37 C. M. Rocha and A. J. Varandas, *Comput. Phys. Commun.*, 2021, **258**, 107556.
- 38 C. Rocha and A. Varandas, *J. Phys. Chem. A*, 2019, **123**, 8154–8169.
- 39 F. G. D. Xavier, M. M. González and A. Varandas, *J. Phys. Chem. A*, 2019, **123**, 1613–1621.
- 40 F. G. D. Xavier and A. Varandas, *Mol. Phys.*, 2021, **119**, e1904157.
- 41 G. D. Xavier, *Comput. Phys. Commun.*, 2022, 108419.
- 42 G. H. Peslherbe, H. Wang and W. L. Hase, *Adv. Chem. Phys.*, 1999, **105**, 171–201.
- 43 J. Li, P. J. Caridade and A. J. Varandas, *J. Phys. Chem. A*, 2014, **118**, 1277–1286.
- 44 H. J. Werner, P. J. Knowles and G. Knizia, *MOLPRO, version 2015.1, a package of ab initio programs*, University of Cardiff Chemistry Consultants (UC3), Cardiff, Wales, UK, 2015.
- 45 H.-J. Werner, P. J. Knowles, F. R. Manby, J. A. Black, K. Doll, A. Heßelmann, D. Kats, A. Köhn, T. Korona and D. A. Kreplin, *et al.*, *J. Chem. Phys.*, 2020, **152**, 144107.
- 46 P. J. Knowles and H.-J. Werner, *Chem. Phys. Lett.*, 1985, **115**, 259–267.
- 47 H.-J. Werner and P. J. Knowles, *J. Chem. Phys.*, 1988, **89**, 5803–5814.
- 48 P. J. Knowles and H.-J. Werner, *Chem. Phys. Lett.*, 1988, **145**, 514–522.
- 49 J. M. Martin and O. Uzan, *Chem. Phys. Lett.*, 1998, **282**, 16–24.
- 50 T. H. Dunning Jr, K. A. Peterson and A. K. Wilson, *J. Chem. Phys.*, 2001, **114**, 9244–9253.
- 51 D. E. Woon and T. H. Dunning Jr, *J. Chem. Phys.*, 1993, **98**, 1358–1371.
- 52 A. Karton and J. M. Martin, *Theor. Chem. Acc.*, 2006, **115**, 330–333.
- 53 A. Varandas, *J. Chem. Phys.*, 2007, **126**, 244105.
- 54 C.-L. Yang, Y.-J. Huang, X. Zhang and K.-L. Han, *THEO-CHEM*, 2003, **625**, 289–293.
- 55 K.-P. Huber, *Molecular spectra and molecular structure: IV. Constants of diatomic molecules*, Springer Science & Business Media, 2013.
- 56 Y. Gao and T. Gao, *Spectrochim. Acta, Part A*, 2014, **118**, 308–314.
- 57 R. Ram and P. Bernath, *J. Mol. Spectrosc.*, 1996, **176**, 329–336.
- 58 Y.-R. Luo, *Comprehensive handbook of chemical bond energies*, CRC Press, 2007.
- 59 I. Dabrowski, *Can. J. Phys.*, 1984, **62**, 1639–1664.
- 60 E. Roueff, H. Abgrall, P. Czachorowski, K. Pachucki, M. Puchalski and J. Komasa, *Astron. Astrophys.*, 2019, **630**, A58.
- 61 J. Langleben, J. Tennyson, S. N. Yurchenko and P. Bernath, *Mon. Not. R. Astron. Soc.*, 2019, **488**, 2332–2342.
- 62 J. Li and A. J. Varandas, *J. Phys. Chem. A*, 2012, **116**, 4646–4656.

- 63 A. Kramida, Y. Ralchenko and J. Reader, *et al.*, National Institute of Standards and Technology, 2018.
- 64 R. J. Le Roy, *J. Quant. Spectrosc. Radiat. Transfer*, 2017, **186**, 167–178.
- 65 F. Genova, D. Egret, O. Bienaymé, F. Bonnarel, P. Dubois, P. Fernique, G. Jasiewicz, S. Lesteven, R. Monier and F. Ochsenbein, *et al.*, *Astron. Astrophys., Suppl. Ser.*, 2000, **143**, 1–7.
- 66 F. Eckert, P. Pulay and H.-J. Werner, *J. Comput. Chem.*, 1997, **18**, 1473–1483.
- 67 M. Semenov, N. El-Kork, S. N. Yurchenko and J. Tennyson, *Phys. Chem. Chem. Phys.*, 2021, **23**, 22057–22066.
- 68 A. Varandas, *Chem. Phys. Lett.*, 1987, **138**, 455–461.
- 69 M. Graff and A. Wagner, *J. Chem. Phys.*, 1990, **92**, 2423–2439.
- 70 K. J. Laidler, *Pure Appl. Chem.*, 1996, **68**, 149–192.